Membrane-tethered cadherin substrates reveal actin architecture at adherens junctions

Sayantika Ghosh*[#1], John James*[1], Badeer Hassan Ummat[1], Darius Vasco Köster[1]

[1]*University of Warwick, Warwick Medical School - Division of Biomedical Sciences and Centre for Mechanochemical Cell Biology, CV4 7AL, Coventry, UK*

**contributed equally*

[#]*current affiliation: University of Cambridge, Department of Biochemistry, Sanger Building, 80 Tennis Court Road, Cambridge, CB2 1GA*

Abstract

Adherens junctions (AJs) are E-cadherin-based adhesions at cell-cell contacts that connect the actin cytoskeleton of epithelial cells. Formation and maturation of these junctions is important in development, e.g. for the generation of epithelial tissues, and loss of adherens junctions is linked to metastasis in cancer. It is well established that AJ formation is a mechano-sensitive process involving cis and trans clustering of E-cadherin and the mechanotransducive activation of α-catenin that connects E-cadherin with the actin cytoskeleton. However, how mobility of E-cadherin in the cell membrane and their local density influences actin polymerisation is less well understood, due to limitations in controlling physical properties of cell membranes and performing high-resolution microscopy in model organisms or cell-monolayers. Here we place MCF7 cells labelled with fluorescent actin, E-cadherin and α-catenin, on fluid supported lipid bilayers (SLB) containing the extracellular domain of E-cadherin, as a biomimetic system enabling super-resolution microscopy of AJs. We found that MCF7 cells were able to attach and spread on these substrates, recruiting E-cadherin and α-catenin to form AJs that can mature and are mobile. Interestingly, we found that depending on E-cadherin mobility within the SLB, distinct types of actin architecture emerge. Low mobility substrates support formin-based linear actin polymerisation while high mobility substrates support Arp2/3-based branched actin network polymerisation. These polymerising actin structures are spatially confined to regions of low E-cadherin density suggesting they play a role in AJ repair. Following how these actin structures at the cell-SLB interface evolve over time indicates regions of both linear and branched actin being present at mature cell-cell contacts.

Introduction

Cells in epithelial tissues are held together by adherens junctions (AJs) formed by E-cadherin interactions at the apical pole of the cell. These structures serve as mechanical anchors and contact points for biochemical and mechanical signalling. Mechano-signalling from AJs is essential to regulate cellular processes like migration and proliferation(Friedl and Mayor 2017). The mechanical forces generated and sensed by these structures depend on the architecture of the underlying actin cytoskeleton (Charras and Yap 2018; Arslan et al. 2021).

AJs are formed when the extracellular domains of E-cadherin from adjacent cells interact with each other. In turn, the intracellular domains of E-cadherin recruit β-catenin which binds to the head domain of α-catenin. Together these proteins form a complex called the cadherin-catenin-complex (CCC), which is the structural unit of an AJ (Mège and Ishiyama 2017). The tail domain of α-catenin can then bind to actin filaments forming a link between the actin cytoskeleton of adjacent cells. Actin in conjunction with myosin can exert a pulling

force on the CCC, unfurling α-catenin to reveal cryptic binding sites for vinculin (Yao et al. 2014). Vinculin not only reinforces the AJs by binding simultaneously α-catenin and actin, but also contributes to actin bundling, potentially by dimerization of its tail domain (Jannie et al. 2015). This intracellular recruitment of proteins promotes clustering of E-cadherin via their extracellular domains, by both cis-clustering within one plasma membrane and trans-clustering of E-cadherins on the plasma membranes of adjacent cells (Thompson et al. 2021). The classical view of a mature cell-cell contact has linear actin bundles stretched taut between AJs parallel to the cell contact (Cavey and Lecuit 2009). The cell membranes are held together by extracellular E-cadherin interactions and the tension across these actin bundles. A combination of cadherins being internalised in vesicles and flowing in from the surrounding membrane, along with the recruitment of actin modulating proteins constantly replenishes and maintains these AJs (Reynolds 2010).

Actin is a globular protein that under the right conditions can self-polymerise into actin filaments. The formation of an actin trimer for nucleation is the rate limiting step for polymerisation, and actin nucleation factors like formins and Arp2/3 promote or mimic the formation of this trimer and give rise to different actin architectures within the cell (Fritzsche et al. 2013). Formins are a family of proteins that can initiate de-novo actin polymerisation by promoting actin nucleation as well as the elongation of existing actin fibres(Oosterheert et al. 2024). Arp2/3 is a protein complex that binds existing actin filaments and mimics an actin trimer to create a branch by allowing for linear polymerisation at a 70 angle from the mother filament(Papalazarou and Machesky 2021). Since both the mother and daughter filaments can be substrates for further branch formation, the combination of branched and linear actin polymerisation can lead to an exponentially expanding actin network that a cell utilises to generate pushing forces (Achard et al. 2010). Actin polymerisation is spatially and temporally controlled by modulating the concentration of proteins that support actin polymerisation in different cellular compartments (Pollard 2016). Linear actin nucleators and elongation factors such as the formins, Formin1, mDia1 and FMNL2 as well as mENA/Vasp have been reported to be present at AJs (Kobielak et al. 2004; Acharya et al. 2017; Grikscheit et al. 2015; Oldenburg et al. 2015). The branched actin network nucleator Arp2/3 along with its activators RAC1, WAVE, IQGAP2 and cortactin are also recruited to AJs (Braga et al. 1997; Han et al. 2014; Noritake et al. 2004).

Although actin polymerisation at AJs was first reported decades ago (Vasioukhin et al. 2000), its effects at AJs are still not entirely clear. The initial study suggested that polymerisation from AJs sustained the linear bundles of actin present at mature cell-cell contacts. Branched actin polymerisation also plays an important role in newly forming cell-cell contacts (Lee et al. 2016), with branched actin networks being remodelled into linear bundles by debranching proteins like Coronin1B (Michael et al. 2016) and actin bundling proteins like nonmuscle myosin IIB and eplin (Abe and Takeichi 2008; Yu-Kemp et al. 2021). More recent studies have found branched actin networks at mature cell-cell contacts and the authors propose that actin polymerisation could function as a mechanism of repair if AJs are disassembled (J. X. H. Li et al. 2021; 2020). Since AJs are constantly maintained structures, it is unsurprising that formation and repair (or re-formation) may be governed by the same mechanism. Indeed, an increase in branched actin polymerisation at AJs has been consistently correlated with increased junction integrity (Senju et al. 2023; Moztarzadeh et al. 2024; James et al. 2025). Testing such hypotheses, has however been challenging, due to the limitations of modern imaging techniques and the position of AJs in cell monolayers and tissues.

Since AJs form between cells at the apical pole of epithelial monolayers, high and super-resolution, live cell imaging capturing the dynamics of the molecular components of AJs has proved difficult, particularly when it comes to resolving dynamics along the cell-cell contact

plane. Attempting to overcome these drawbacks, several studies have imaged cells adhering onto E-cadherins immobilised on coverslips (Bertocchi et al. 2017; Schimmel and Noordstra 2023; Collins et al. 2017), but these systems offer limited insights into AJ formation as important aspects such as lateral mobility of E-cadherin and its clustering cannot be properly studied. Alternatively, E-cadherin molecules tethered to supported lipid bilayers formed on glass coverslips represent a readily available system to incorporate these parameters (Biswas et al. 2015; 2016). This system is designed for the study cell adhesion dynamics in live cells and a recent study has revealed how actomyosin flows are coupled with E-cadherin during the first hour of adhesion in zebrafish ectoderm progenitor cells (Arslan et al. 2024).

In the present study, we employ the powers of SLBs decorated with the E-cadherin extracellular domain (E-cadECD) to study the organisation of the actin network, E-cadherin and α-catenin in MCF-7 cells, a cell line derived from breast cancer tissue and commonly used to study E-cadherin based cell-cell adhesion (Noordstra et al. 2023). Using total internal reflection fluorescence (TIRF) and TIRF- structural illumination microscopy (SIM) we follow protein dynamics during AJ formation and maturation up to five hours post adhesion. We were able to recapitulate previously reported characteristics of AJs to confirm the relevance of our model system. We discovered that E-cadherin mobility and density direct the formation of regions at the cell-SLB interface that are dominated by either Arp2/3 or formin driven actin polymerisation. Our results indicate that that cells can sense ligand mobility on their neighbours to direct actin polymerisation at AJs.

Results

MCF7 cells form adherens junctions on SLBs containing E-cadECD

MCF7 E-cadherin-GFP knock in cells expressing LifeAct-TagRFPT and iRFP670-α-catenin (Noordstra et al. 2023) were plated on supported lipid bilayers (98% DOPC, 2% NiNTA-DGS) decorated with His_6-E-cad-ECD (Fig. 1a, Supp Video 1). TIRF imaging revealed that MCF7 cells can attach and spread on these substrates (Fig. 1 b). The cell spreading area increases during the first 60 min and then plateaus at 69 (±17) μm^2, indicating that cell spreading reaches a steady state within an hour (Fig 1c). As reported earlier, cell spreading is driven by actin rich protrusions that grow from the edge of the cell along the SLB. Although the protrusion area decreases over time they persist once the cell has reached its maximum spreading area (Fig. 1 d, Supp. Fig. 1). Together with actin, E-cadherin and α-catenin are recruited to the SLB facing surface of the cell showing that AJs are being formed at the cell-SLB interface (Fig. 1 e-g). Interestingly, the recruitment of AJ proteins continues even after the end of cell spreading suggesting that new AJ formation and maturation can possibly be visualised at later time points.

To this end, we utilised TIRF-SIM imaging to obtain super-resolution images of AJs at different stages of maturation (Fig 2a). At the edge of protrusions, we found E-cadherin puncta at the tips of actin bundles that are stable over tens of seconds of imaging (green arrows). Since TIRF-SIM only excites fluorophores within the first ~100 nm above the surface of the coverslip, these structures are presumably points of attachment to the E-cadECD-SLB substrate. These early adhesions are characterised by the presence of E-cadherin but no detectable α-catenin (green arrows). Following these adhesions over time reveals the elongation of E-cadherin signal (yellow arrows) indicating further clustering of E-cadherin along actin protrusions as well as the recruitment of α-catenin (red arrows), which are hallmarks of the maturation of cadherin puncta into AJs. Within the protrusion, we see that the position of AJs changes over time (Fig 2b), suggesting that they bind to the actin cytoskeleton within the protrusions. Tracking these AJs shows that they move retrogradely from the tip of the protrusion to the base, along actin filaments leading to further clustering

(Fig 2c, d, Supp Video 2). Concomitantly, at the base of the protrusion, we see an enrichment of mature AJs indicated by an increase in actin, E-cadherin and α-catenin (Fig 2a, cyan arrows). This enrichment leads to the formation of an actin ring at the perimeter of the cell (Supp Fig 2 a, b) that has been reported previously (Arslan et al. 2024) and is reminiscent of the apical actin ring found in epithelial monolayers. Thus, we demonstrate here that our cell-SLB system recapitulates key features seen in physiological AJs – a) AJs start as E-cadherin puncta and mature into complexes that contain a-catenin, b) AJs are motile along actin bundles, c) Retrograde flow of AJs enhances clustering (Noordstra et al. 2023).

Actin architecture at the cell-SLB interface

Next, we looked at the cell interior as a model for mature cell-cell contacts that have been in contact with the SLB for an extended period of time (>1hr) (Fig. 3a). We found that the actin architecture is very different from cells plated on glass coverslips coated with immobile E-cadherin substrates (Collins et al. 2017), with the absence of stress fibres being the most striking observation (Fig. 3b). This suggests, as expected, that mobility of E-cadherins is an important factor in the physiological functioning of AJs. We found actin rich structures that we classify into four different types of actin organisation - disperse actin, retrograde flow, actin bundles and actin patches (Fig. 3c, Supp Video 3). Retrograde flow is found at the cell edge and in protrusions, which is similar to observations of cells plated on substrates with immobilised E-cadherin or extra-cellular matrix proteins. The E-cadherin distribution in this region is characterised by the aforementioned E-cadherin puncta at the tips of protrusions and mature AJs at the base (Fig. 3c). We plotted the intensities of actin and E-cadherin within 250 nm windows in this region to study their colocalization (Supp. Fig. 2c), and on average these regions contained by far the highest densities of E-cadherin and actin (Fig. 3d). Plotting a linear regression line reveals a high correlation between E-cadherin and actin intensities confirming that they colocalise in these structures (Supp. Fig. 2d).

Surprisingly we found that in the cell interior, not all actin and E-cadherin were well co-localised and many regions rich in E-cadherin did not recruit actin. Disperse actin is scattered throughout the cell interior (Fig. 3c) and does not seem to be affected by E-cadherin distribution (Supp. Fig. 2d). Actin bundles appear in spatially delimited regions and unlike disperse actin are not mobile (Fig. 3e). Both static bundles and disperse actin seem to be distinct from stress fibres observed in cells on immobilised e-cadherin and extra-cellular matrix, as they do not show the characteristic low curvature expected for fibres under tension (Supp. Fig. 2f). Actin patches are characterised by their actin filament organisation changing over short timescales and that they do not show any long linear actin structures (Fig 3e). Perhaps most interestingly, both actin bundles and actin patches are formed in regions of decreased E-cadherin (Fig. 3d) suggesting they are formed in regions where AJs are not well assembled.

Prolonged illumination of fluorophores leads them to going into a dark state, and not emitting photons, which is typically known as photobleaching. By quantifying the rate of photobleaching in different actin structures we could assess quantitatively how quickly these structures remodel and incorporate new fluorescent actin probes (Fig. 3c, d). Disperse actin has the highest photo-bleaching rate, about 1.7 times faster than actin bundles (Fig. 3 f,g). This indicates that actin bundles are actively maintained structures with the actin polymerisation constantly delivering new LifeAct-TagRFPT. The lowest photobleaching rates are found in regions of retrograde flow and actin patches (2.4 times slower than disperse actin), suggesting a faster mode of actin filament renewal and remodelling than in actin bundles (Fig. 3 f,g). Taken together with the formation of actin bundles and patches at

regions of low E-cadherin density, this data suggests that actin polymerisation is favoured at regions of cell-cell contacts where AJs are not well established.

Branched and linear actin polymerisation are differentially regulated by cadherin mobility

Given the linear appearance of the actin bundles, we hypothesised that they are maintained by formin-mediated linear polymerisation of actin filaments. In contrast, based on studies on cells adhering onto extracellular matrix substrates, we assume that retrograde flow at in cells adhering to E-cadherin decorated SLBs is controlled by Arp2/3-mediated branched actin polymerisation (Yang et al. 2012). . Dynamic patches show similar characteristics to retrograde flow, both visually and in terms of actin photobleaching, suggesting they are also maintained by Arp2/3. This would explain the lower photobleaching rates in retrograde flow and dynamic patches compared to bundled actin, as branched actin leads to higher polymerisations rates by affording more actin filaments to be elongated by linear polymerisation (Achard et al. 2010). In a next step, we tested the effect of E-cadECD lateral mobility on regulating the mode of actin polymerisation by changing the fluidity of the SLB.

We performed TIRF-SIM imaging of cells adhering to E-cadECD decorated SLBs composed primarily of the unsaturated lipid 1,2-dioleoyl-sn-glycero-3-phosphocholine (DOPC), and the saturated 1,2-dipalmitoyl-sn-glycero-3-phosphocholine (DPPC). Using fluorescence recovery after photobleaching (FRAP), we determined that the mobility (measured as diffusion constant) of E-cadECD is 17 times higher in DOPC SLBs than in DPPC SLBs (D_{DOPC} = 0.85 (± 0.05) μm^2; D_{DPPC} = 0.05 (± 0.01) μm^2) (Supp. Fig. 3). We first quantified the rate of retrograde flow in protrusions using kymographs and found that the retrograde flow increases 1.5 fold in cells plated on high mobility DOPC SLBs ($v_{DOPC}^{retro} = 15\ (\pm 5)\ \mathrm{nm\ s^{-1}}$) compared to low mobility DPPC SLBs ($v_{DPPC}^{retro} = 10\ (\pm 3)\ \mathrm{nm\ s^{-1}}$) (Fig. 4a, b). Treating cells with the Arp2/3 inhibitor CK-666 resulted in a threefold decrease in retrograde flow ($v_{DOPC,CK666}^{retro} = 5\ (\pm 2)\ \mathrm{nm\ s^{-1}}$). Together these results show that branched actin polymerisation is indeed responsible for maintaining retrograde flow and that Arp2/3 activity is upregulated when engaging with highly mobile E-cadherins.

Next, we analysed actin flows in actin patches under the same contexts. Due to the lack of a clear directionality of actin motion we could not employ the kymograph analysis. Instead, we utilised particle image velocimetry (PIV) to map directional changes of actin signal over time in and around actin patches (Fig. 4c). Even though the apparent actin flow velocities obtained by PIV are typically lower than the ones obtained by kymograph analysis, we could observe a 1.2 fold increase in actin flow velocity in cells on high mobility SLBs ($v_{DPPC}^{patch} = 3.3\ (\pm 0.2)\ \mathrm{nm\ s^{-1}}$; $v_{DOPC}^{patch} = 4.2\ (\pm 0.3)\ \mathrm{nm\ s^{-1}}$) (Fig. 4d). As observed in retrograde flow, actin flow in patches decreased by a factor of 2 in cells treated with CK666 ($v_{DOPC,CK666}^{patch} = 2.3\ (\pm 0.6)\ \mathrm{nm\ s^{-1}}$). This is in line with our hypothesis that these structures are maintained by Arp2/3-mediated branched actin polymerisation which is upregulated by increased E-cadherin mobility.

Last, we quantified actin elongation rates in actin bundles by generating kymographs along the direction of extension (Fig. 4e, Supp. Fig. 2e, Supp. Video 4). Interestingly, we found that actin bundles show a faster elongation rate in cells on DPPC SLBs, ($v_{DPPC}^{bundle} = 6\ (\pm 2)\mathrm{nm\ s^{-1}}$) compared to DOPC SLBs ($v_{DOPC}^{bundle} = 4\ (\pm 1)\mathrm{nm\ s^{-1}}$), and that the rate decreased threefold when cells were treated with the formin inhibitor SMIFH2 ($v_{DPPC,SMIFH2}^{bundle} = 2\ (\pm 1)\mathrm{nm\ s^{-1}}$) (Fig. 4f). This confirms that static bundles are indeed maintained by formin-mediated linear actin polymerisation. The higher bundle elongation

rate in cells on DPPC SLBs suggests that formin-mediated linear actin polymerisation is upregulated when E-cadherin mobility is increased. Taken together these results predict that an increase in E-cadherin mobility leads to activation of Arp2/3 and a shift from linear polymerisation alone to a combination of branched and linear polymerisation.

Since actin bundles and patches are both formed in regions of low cadherin intensity, we explored the possibility they may be interconvertible actin structures. We detected and quantified the area occupied by actin bundles in cells where bundles and patches were present. We detected fewer actin bundles over time (Fig. 5b) and the relative area of E-cadherin-deficient regions occupied by the bundles decreases over time (Fig. 5c). Concomitantly, we found that identifiable actin fibres covered a larger relative area of E-cadherin-deficient regions at 4h compared to 5h post seeding (Supp. Fig. 4a, b). This suggests that static actin bundles are replaced by more dynamic actin structures and that branched actin polymerisation may be adding to the linear polymerisation that maintains bundles, to convert them into dynamic structures as the cell-cell contact matures.

Next, we looked at how these branched and linear networks develop over time. We plated cells on high mobility SLBs decorated with E-cadECD and imaged them over 5 hours post seeding (Fig 5c). We quantified areas of the cell showing different types of the above defined actin architectures (Fig. 5d). At 1h post seeding, we see disperse actin in the interior of the cell and retrograde flow at the cell edge, with large protrusions as the cell is still spreading. At 2 hours post seeding, we see that most of the cell area is covered with static actin bundles and no detectable protrusions. Small areas between the bundles display a more disperse actin network, and at 4h post seeding the disperse filaments take up a larger area and separate the actin bundles into compartments. 5 h post seeding, these static bundles are replaced by dynamic patches of actin. Together these results give us an idea of how branched and linear actin polymerisation are regulated over the course of cell-cell contact maturation. The starting stages of cell-cell contact formation involve both branched and linear actin networks (Fig. 5f). Linear networks seem to predominate at later stages of maturation after which branched networks become active again, possibly as a mechanism for constant maintenance/repair.

Discussion

We have shown here that our system is apt for imaging mobile AJs using super-resolution TIRF-SIM. We have shown that increase in cadherin mobility favours Arp2/3 activity while a decrease in cadherin mobility favours linear actin polymerisation by formins. We have also shown that regions of relatively lower cadherin recruitment develop polymerising linear actin structures that then transition into branched networks. We analysed temporal changes in actin architecture and found them consistent with previous reports of actin and its polymerisation factors at AJs. Early cell-cell contacts are enriched in branched actin which is reorganised into linear bundles (Lee et al. 2016; Michael et al. 2016). This switch from branched to linear actin networks is also evident from the initial TIRF experiments where we see a decrease in protrusion size consistent with a decrease in Arp2/3 activity after 1h post attachment. The reemergence of actin polymerisation and branched actin networks at later stages is also consistent with recent studies showing that Arp2/3 reappears at late cell-cell contacts, potentially as a mechanism for repair (J. X. H. Li et al. 2021; 2020). *In vivo*, we would expect that regions with a loss of cell-cell contact would exhibit lower cadherin density due to loss of cadherin clustering and higher cadherin mobility due to detachment of AJs from the actin network. Indeed, in such conditions, we do see an increase in actin polymerisation and the presence of branched actin networks.

The actin architecture we see 1h post seeding is remarkably similar to those reported in zebrafish ectoderm progenitor cells at the same time point (Arslan et al. 2024). This suggests that the processes we are studying are conserved across cell lines and species. We have additionally studied the progress of this actin architecture as the cell-cell contact evolves over time and observed intricate, dynamic structures that help us better understanding spatially heterogeneous actin polymerisation dynamics. The same study also reports a flow of actin along with actin binding proteins myosin and ezrin from the cell interior to the periphery creating an actin ring. Consistently, we observe a flow of actin and AJs from protrusions inwards to the periphery of the cell cortex where we see the formation of the actin ring. Whether this actin ring is analogous to the actin ring connecting AJs in a tissue is questionable. In tissues, cells are polarised, and the actin ring and AJs are concentrated at the apical pole. This further raises the question of whether the increase in area of AJ formation in our system depletes the density of E-cadherin to a level that is physiologically inaccurate. Further studies introducing a polarising stimulus are essential to establish this system as a physiologically relevant model.

Using TIRF-SIM super-resolution imaging of the cell-SLB interface at later time points (>2h post seeding) has revealed interesting and exciting actin network dynamics with the appearance of dynamic actin patches and regions of seemingly stable actin bundles. First, we find that both dynamic patches and areas of retrograde flow behave similarly in all measures we have studied. This suggests that they are maintained by the same processes, activation of Arp2/3, likely by the Rac1 pathway, which mediates polymerisation of branched actin networks (Lee et al. 2016). On the other hand, actin bundles are maintained by formins that could be activated by the RhoA pathway as observed in integrin-mediated focal adhesion formation (Kalappurakkal et al., *Cell,* 2019). The fact that dynamic patches and static bundles appear as spatially confined structures along the cell-SLB interface and change over time suggests that RhoA and Rac1 linked pathways are confined in local zones along the cell-SLB interface (Yamada and Nelson 2007). Interestingly, the mobility of E-cadECD, and with this the amount of traction force that cells generate when dragging E-cadherin along the cell surface, could be a regulating factor for the type of actin structure generation. Global regulation of RhoA during the first hour of cell-SLB adhesion was recently reported (Arslan et al. 2024), however, our novel discovery of local zones with distinct actin patterns opens the path to investigate the biochemical and physical mechanisms allowing the cell to sense local differences in E-cadherin mobility.

Acknowledgements

The authors thank Prof. Marco Fritzsche and Dr. Helena Coker (Kennedy Institute of Rheumatology, University of Oxford) for granting access and their help and technical support performing the SIM-TIRF experiments, and the Medical and Life Science Research Fund for financial support of these experiments. **SG** and **BHU** would like to thank the University of Warwick International Chancellor's fellowship for supporting their research. **JJ** and **DK** are supported by an EPSRC grant (EP/V043498/1).

Materials and Methods

Preparation of Supported Lipid Bilayers and Experimental Chambers

Supported lipid bilayers and the experimental chambers were prepared as described earlier(Köster et al. 2022). Glass coverslips (25 mm diameter, #1.5 borosilicate, Gerhard Menzel GmbH, cat. no. LDRND25/1.5) for SLB formation were cleaned with 2% Hellmanex

III solution (Hellma Analytics, cat. No. Z805939, Merck) following the manufacturer's instructions, thoroughly rinsed with MilliQ water, then placed in a 3M KOH (Sigma-Aldrich) solution and sonicated for 15 mins, again thoroughly rinsed with MilliQ water and finally blow dried under a stream of N2 gas.

Experimental chambers were made by cutting off the lid and conical bottom part of 0.2 ml PCR tubes (cat. no. I1402-8100, Starlab) and sticking the remaining cylinder onto the cleaned coverslip glass using UV glue (cat. no. NOA88, Norland Products) and three minutes curing by intense UV light at 265 nm (UV Stratalinker 2400, Stratagene). Freshly cleaned and assembled chambers were directly used for experiments.

Supported lipid bilayers (SLB) containing 96% of DOPC lipids (cat. no. 850375, Avanti Polar Lipids) for high mobility membranes or DPPC lipids (cat. no. 850355P, Avanti Polar Lipids) for low mobility membranes and 4% DGS-NTA(Ni2+) lipids (cat. no. 790404, Avanti Polar Lipids) were formed by fusion of small uni-lamellar vesicles (SUV) that were prepared by lipid extrusion using a membrane with 100 nm pore size (cat. no. 610000, Avanti Polar Lipids). SLBs were formed by addition of 10 µl of SUV mix at 4 mM lipid concentration to chambers filled with 90 µl SLB buffer (1xTBS solution, pH 7.4), incubated for 25 min and then washed 10 times with SLB buffer. Extrusion and SLB formation were performed at RT for the DOPC containing lipid mix and at T = 40-45˚C for the DPPC containing lipid mix to ensure formation of uniform lipid bilayers.

Glass slides were mounted into AttoFluor metal chambers (cat. no. A7816, Invitrogen) for imaging on inverted microscopes. For live cell imaging using TIRF-SIM, no small chambers were used and SLBs were formed on the entire glass coverslip. Cleaned glass coverslips were mounted into AttoFluor chambers and SLB were formed by adding 120ul of SUV was added to 300ul SLB formation buffer.

Cell Culture

MCF 7 E-cad-GFP CRISPR-Cas9 knock in cells transduced with LifeAct-TagRFPT and iRFP670-α-catenin were a gift from Ivar Noordstra (Alpha Yap Laboratory). Cells were cultured in Dublecco's Modified Eagle Media (DMEM) with Glutamax (Gibco) supplemented with 10% v/v fetal bovine serum (heat inactivated, cat. no. F4135, Merck), 5% (100 ug/ml) Penicillin/streptomycin, 50 ug/ml Geneticin G418 (cat. no. 10131027, Gibco) and 0.25 ug/ml Puromycin (cat. no. 15490717, Thermo Fisher) at 37 °C with 5% CO2 in a humidified incubator.

Fluorescence Recovery After Photobleaching (FRAP)

We performed FRAP experiments to determine the diffusion rate of histidine-tagged proteins tethered to SLBs of different compositions. SLBs were formed in our PCR-tube based experimental chambers and labelled fluorescently by incubation with 10 nM His6-GFP for 40 min followed by washing off unbound protein (replacement of 50 ul of the old buffer with fresh one for ten times). FRAP image sequences were recorded using a spinning disc confocal microscope (Ultraview Vox, Perkin Elmer) with a 100x objective (NA 1.40, oil, Plan Apo VC, Nikon) and equipped with a FRAP unit. The sample was illuminated, and the image window was adjusted to have uniform illumination. A region of interest of 5 µm diameter was drawn using ROI tool and saved for future use. Photobleaching was performed using the 488 nm laser at maximum power. Acquisition criteria was set to 10 frames before bleaching, and 4 mins of imaging after bleaching at a time interval of 5 s per frame. The same conditions were maintained for all samples. FRAP images were acquired with a Hamamatsu ORCA-R2 camera operated by Volocity 6.0 software (Perkin Elmer).

The mean intensity values of the FRAP region were bleach corrected using the readings of an area outside of the FRAP region and normalised by dividing the mean value from the pre-bleach image sequence. An exponential function was fitted to the recovery curve (T=0 is defined as the end of the bleach procedure), and the resulting time constant was used to calculate the diffusion constant using the equation describing fluorescence recovery of a circular region of radius w: $D = \frac{0.88\, w^2}{4\, \tau_{1/2}}$ (Axelrod et al. 1976).

Total Internal Reflection Fluorescence (TIRF) microscopy

TIRF microscopy is a method of choice to visualize fluorescently labelled objects in the vicinity of a surface while increasing the signal to noise ratio if the bulk phase also contains fluorescent species. TIRF microscopy was performed using a Nikon Eclipse Ti-E/B microscope equipped with perfect focus, a Ti-E TIRF illuminator (CW laser lines: 488 nm, 565 nm, 647 nm) and a Zyla sCMOS 4.2 camera (Andor, Oxford Instruments, UK) controlled by Andor iQ3 software. The TIRF mode was generated by illumination through the periphery of a high NA objective (100X, 1.45 NA).

Extended-Total Internal Reflection Fluorescence – Structured Illumination Microscopy

Super-resolution imaging was performed at 37˚C on a custom-built e-TIRF-SIM microscope in the Kennedy Institute of Rheumatology (University of Oxford). The specifics and theory of e-TIRF-SIM is detailed elsewhere (D.Li et al. 2015). In brief, a spatial light modulator (SLM, Forth Dimension Displays, QXGA3DM) was used to generate diffraction patterns resulting in a numerical aperture of 1.38-1.41 at the objective back aperture. The exact angle was tuned to achieve a penetration depth below 150 nm for each 488, 560, and 640 nm laser lines. Illumination and detection were performed through the same oil objective (Olympus 100x, NA 1.49; UPLAPO100XOHR). Per frame, a total of 9 raw images (200 ms exposure time) were acquired onto two Hamamatsu Orca Flash 4.0 cameras for a single excitation wavelength before switching to the next wavelength. Time-lapses of cell adhesion dynamics were recorded at 10s per frame. Raw images were processed and reconstructed into SIM images by custom made software (D. Li et al. 2015). Illumination path and camera alignment were performed prior to biological experiments by imaging 100 nm Tetraspeck fluorescent beads settled to a coverslip in PBS, in all three excitation colours.

Image analysis

Cell area in TIRF images was calculated by measuring the area of actin staining utilising thresholding in FIJI. Curves were time-shifted to synchronise different fields, considering that cells were fully attached once they reach an area of 20 μm^2. Actin, E-cadherin and α-catenin recruitment show average intensity of signal in this area normalised to the highest average intensity reached in each cell. To calculate protrusion area, cell edges were first segmented using Otsu thresholding and a morphological opening with a 2.68μm filter was applied to generate a smoothened inner edge corresponding to the cell cortex. Protrusion area was then calculated as the area between the detected and smoothed edges.

Rate of photodamage is the rate of decrease in relative actin intensities in manually drawn ROIs containing different actin architectures, normalised to the intensity at the first time-point. Rate of growth of static bundles and rate of retrograde flow were measured from kymographs drawn along the direction of growth and flow respectively. PIV was carried out using PIVLAB in MATLAB. Each point on the graph represents average magnitudes of velocities at all points within a region of dynamic actin, further averaged over 30 time-intervals. Areas of regions containing different actin architectures were estimated by manually drawing ROI in FIJI. For detecting actin bundles, linear structures within manually

drawn ROIs were detected using the Sato tubeness enhancement filter. Actin bundles were then selected after segmentation, by manually setting a threshold at the first time point. Threshold values for subsequent time points were normalised against bleaching across the whole field.

For statistical analysis, populations were first tested for normality using a Shapiro-Wilk test. Difference between means was tested using t-test with Welch's correction for populations conforming to normality and with Mann-Whitney test for population deviating from normality.

Figures

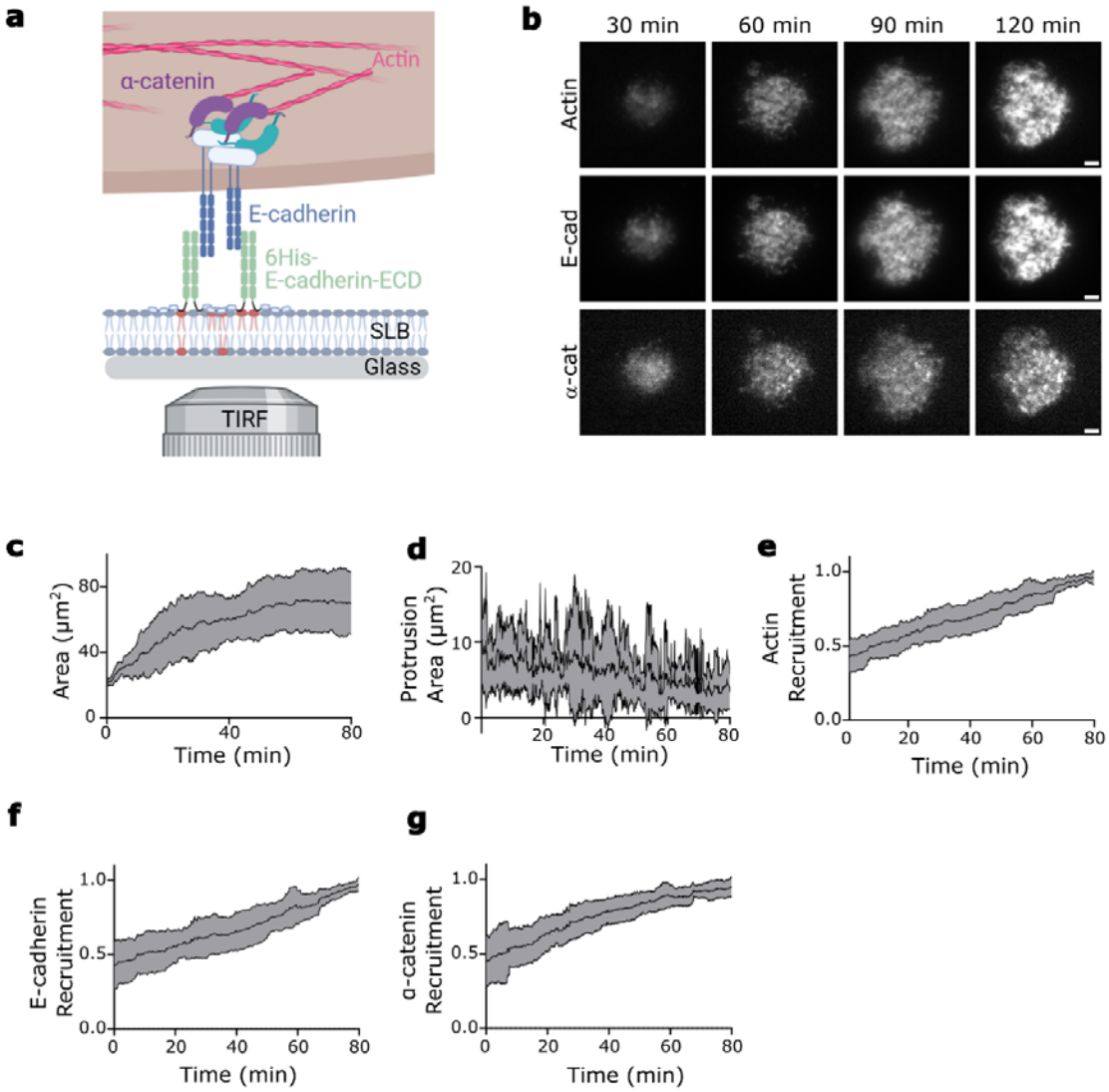

Fig 1: MCF7 cells form AJs on SLBs containing E-cadherinECD **a** MCF7 E-cadherin-GFP knock in cells expressing LifeAct-TagRFPT and iRFP670-α-catenin were plated on SLBs decorated with His_6-E-cadECD. **b** TIRF images of MCF7 cells at indicated times post-seeding; scale bar = 2μm. **c,d** Total area and area of protrusions individual cells spreading over time; mean ± SD plotted n=7. **e-g** Plots of relative intensities of LifeAct-TagRFPT, GFP-E-cadherin, and iRFP670-α-catenin at the cell-SLB interface over time; mean ± SD of n=14.

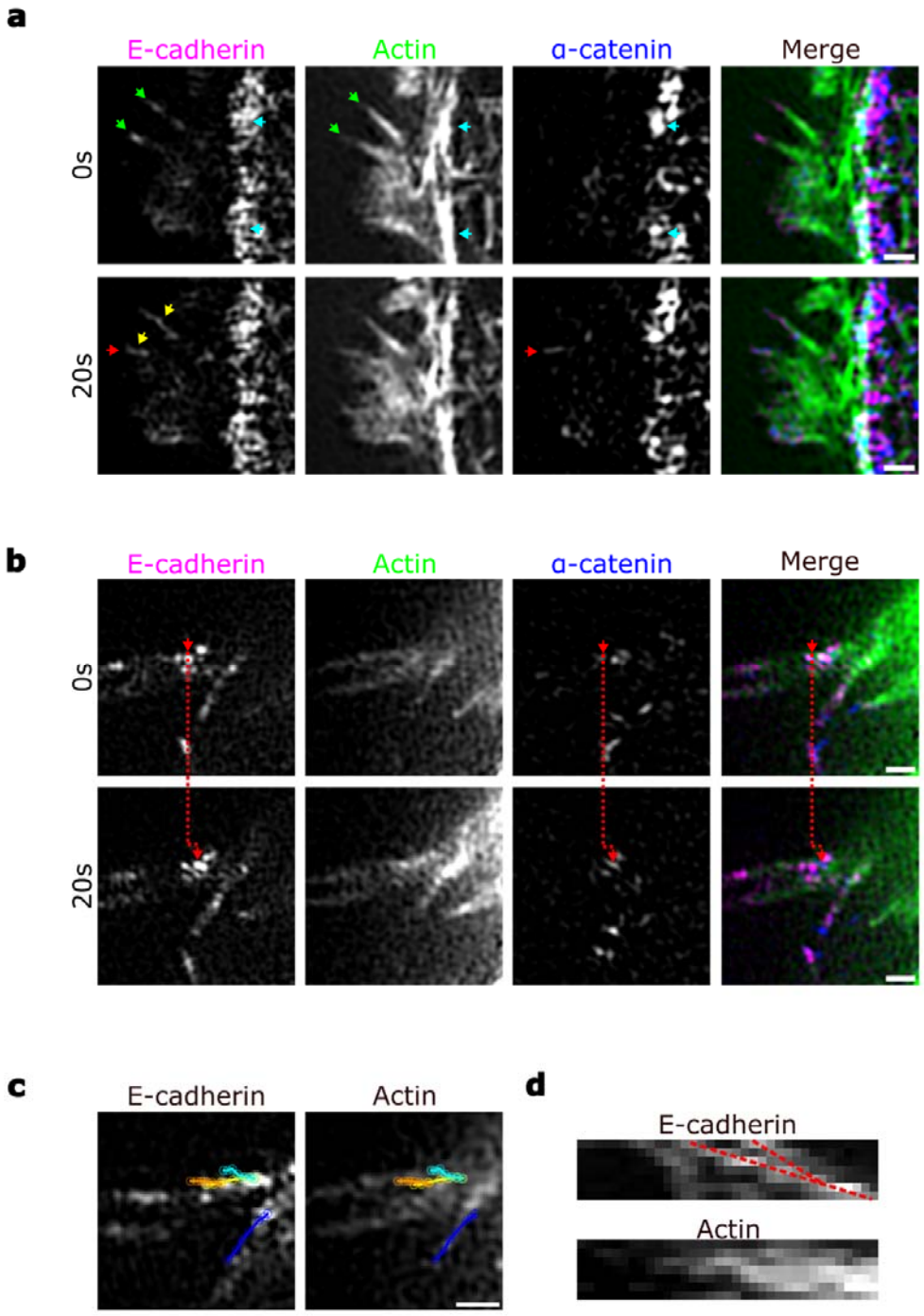

Fig 2: AJs formed on SLBs are mobile structures. a TIRF images of MCF7 cells expressing GFP-cadherin, LifeAct-TagRFPT and α-catenin. Green arrows show E-cadherin recruited to ends of Actin filaments. Yellow arrows show Cadherin staining lengthening along the filament. Red arrow shows α-catenin recruited to E-cadherin enriched structures. Cyan arrows show E-cadherin, α-catenin and actin colocalised in mature AJs. **b** E-cadherin and α-catenin puncta move over time **c** Tracks of E-cadherin puncta moving along actin filament. **d** Kymographs of E-cadherin and actin showing the movement of and clustering of E-cadherin puncta. All scale bars are 0.5μm.

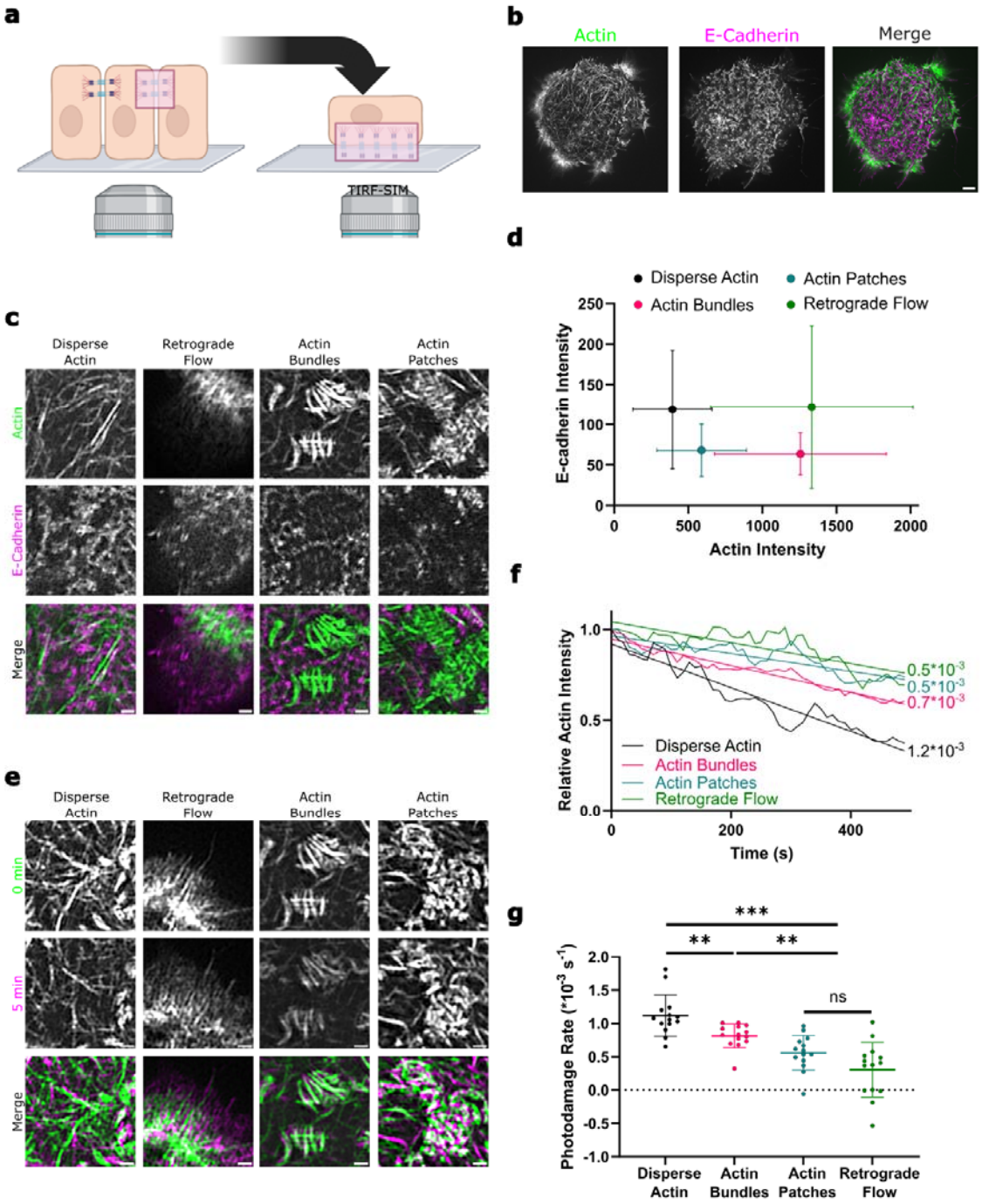

Fig 3: Types of actin architecture at AJs. a AJs are formed at the cell-SLB interface. **b** Sample TIRF-SIM image of a whole cell expressing GFP-E-cadherin and LifeAct-TagRFPT; scale bar=2µm. **c** TIRF-SIM images showing E-cadherin recruitment at regions of different actin architectures; scale bar = 0.5µm. **d** Average intensities of LifeAct-TagRFPT and GFP-E-cadherin in regions of different actin architecture, made by binning 8x8 pixels from TIRF-SIM images to make 250nm windows); mean±SD plotted. **e** TIRF-SIM images of different actin architectures before and after imaging for 5 mins at an interval of 10 s per reconstructed image; scale bar = 0.5 µm. **f** Representative curves of decrease in actin signal intensity over time in different actin architectures. **g** Rate of decrease in actin intensity in regions with different actin architectures; mean ± SD plotted; n=10 from N=2.

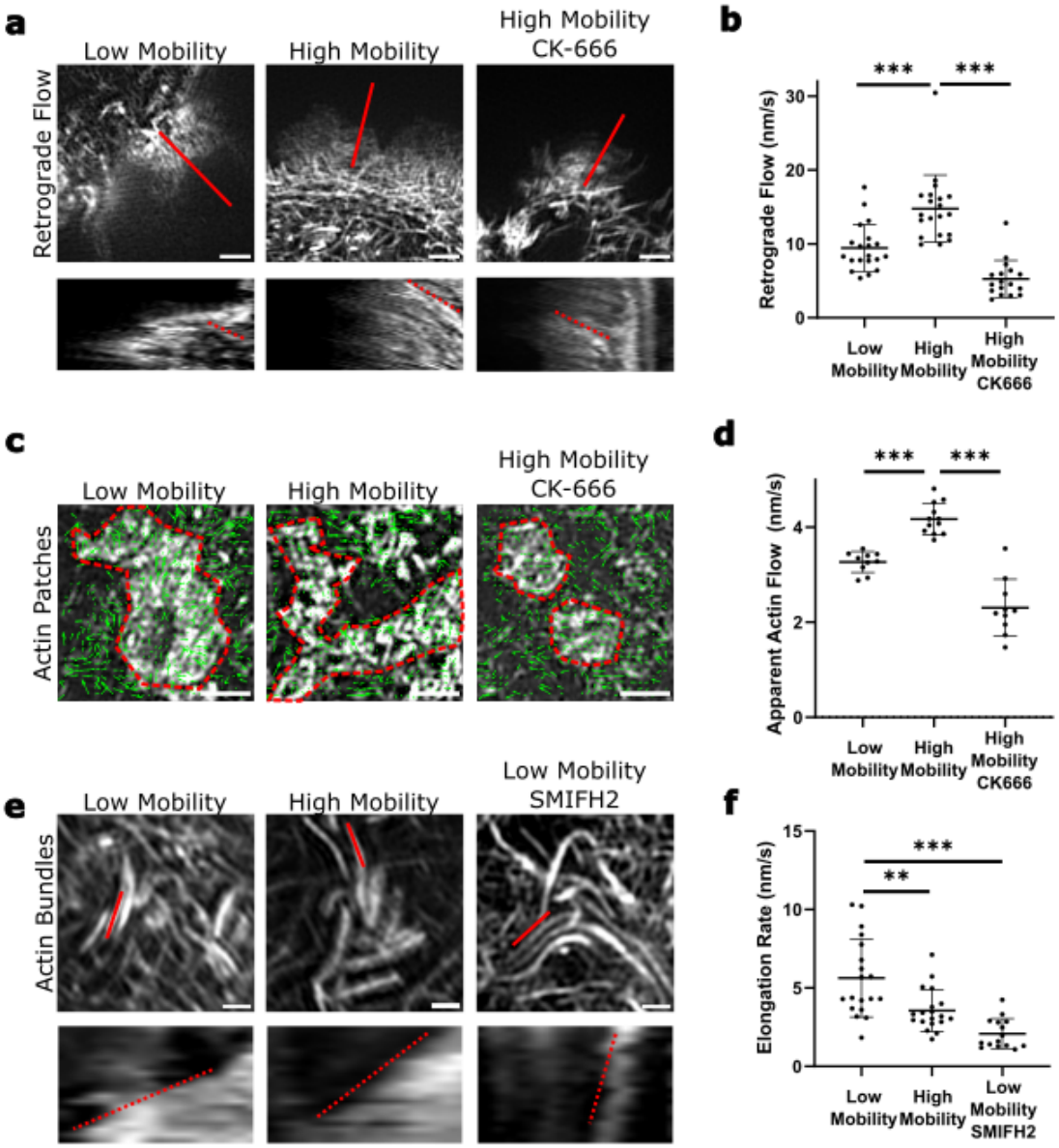

Fig 4: Mobility of cadherin substrate regulates branched and linear actin polymerisation. a Kymographs along the red line give rate of retrograde flow; scale Bar = 1µm. **b** Rates of retrograde flow in cells plated on low and high mobility substrates and in presence of Arp2/3 inhibitor CK666; mean ± SD plotted from N=3. **c** Velocity vectors from PIV analysis used to measure apparent actin flows in dynamic patches; scale Bar = 1µm. **d** Apparent actin flows in dynamic patches in cells plated on low and high mobility substrates and in presence of Arp2/3 inhibitor CK666; mean ± SD plotted from N=3. **e** Kymographs along the red line give rate of actin bundle elongation. **f** Rates of actin bundle elongation in cells plated on low and high mobility substrates and in presence of formin inhibitor SMIFH2; mean ± SD plotted from N=3.

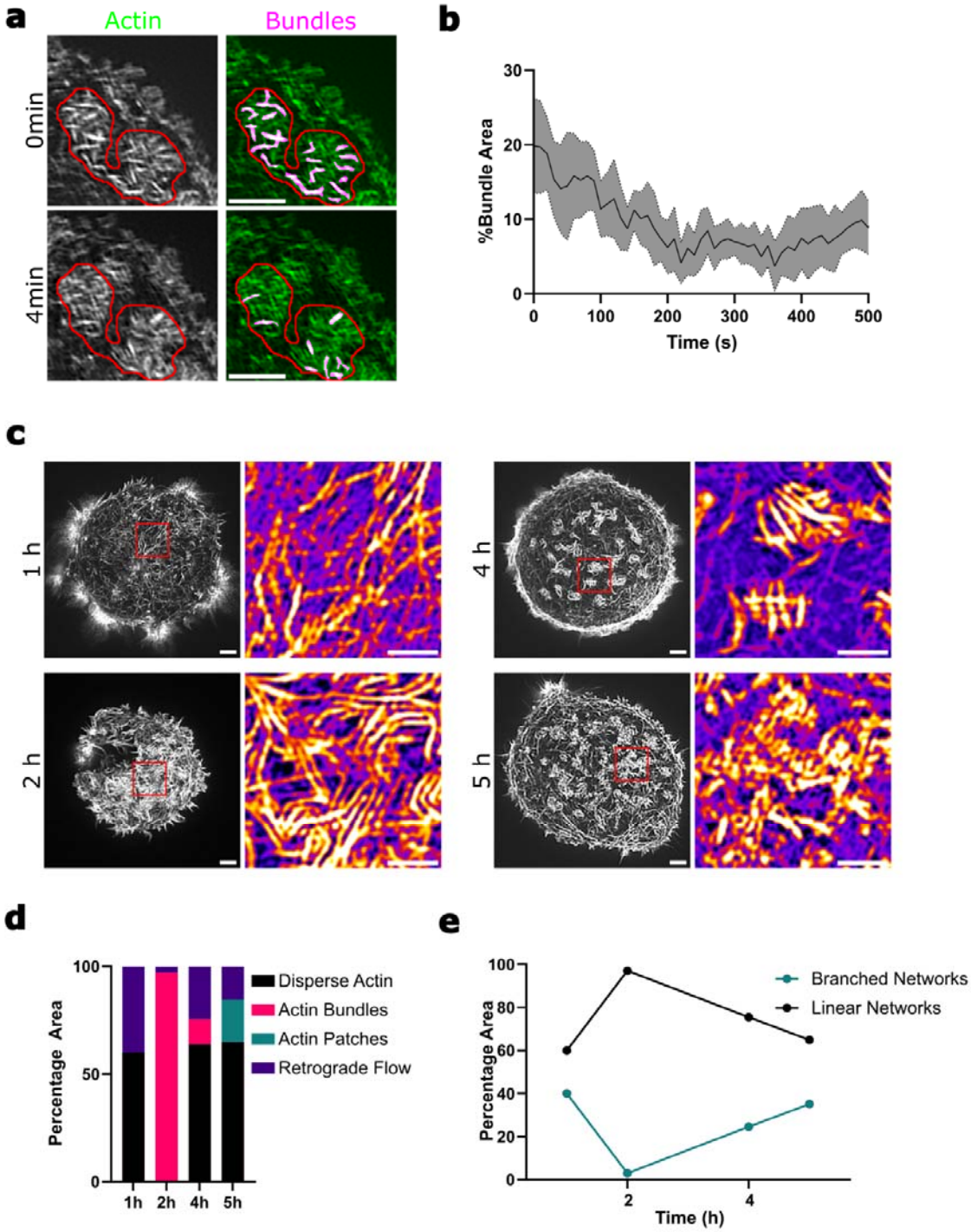

Fig 5: Branched and linear actin polymerisation are temporally regulated during AJ maturation a TIRF-SIM images of actin and detected actin bundles; scale Bar = 1µm. **b** Percentage of area occupied by actin bundles in E-cadherin deficient regions over time. **c** TIRF-SIM images of actin in MCF7 cells imaged at different times post-seeding; scale Bar = 2µm. **d** Percentage Area of the cell covered by varying actin architectures at different times post seeding. **e** Percentage Area of the cell covered by branched and linear actin networks at different times post seeding; one representative cell each from N=3.

Supplementary Figures

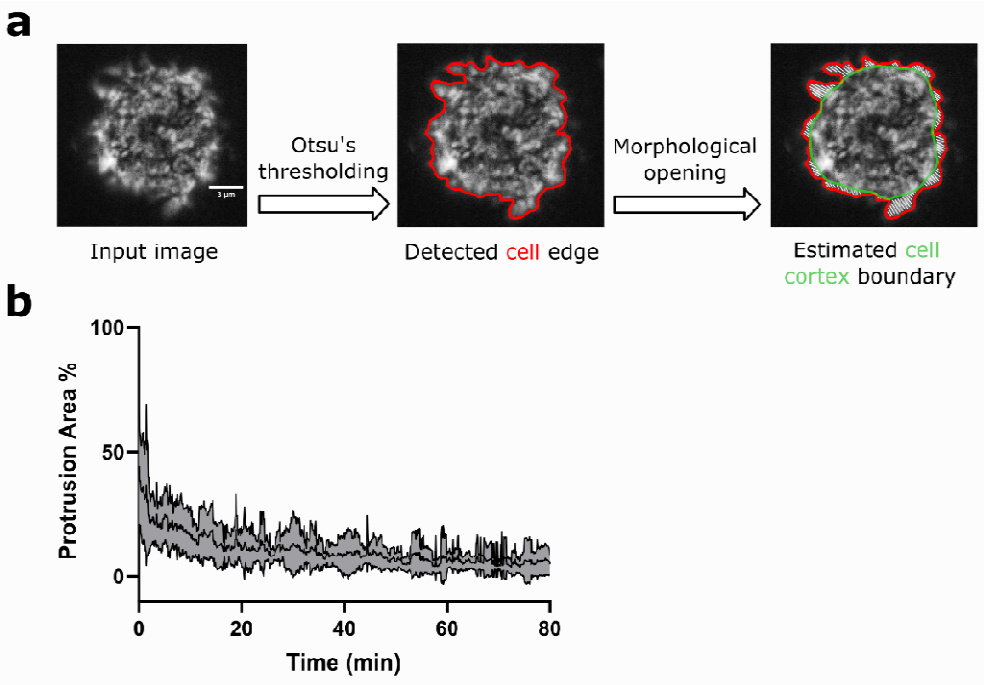

Supp Fig 1: a Protrusion area is calculated as the area between detected edge of the cell (Red) and the estimated edge of the cortex (Green). **b** Decrease in protrusion area over time shown as a percentage of total area occupied by a cell.

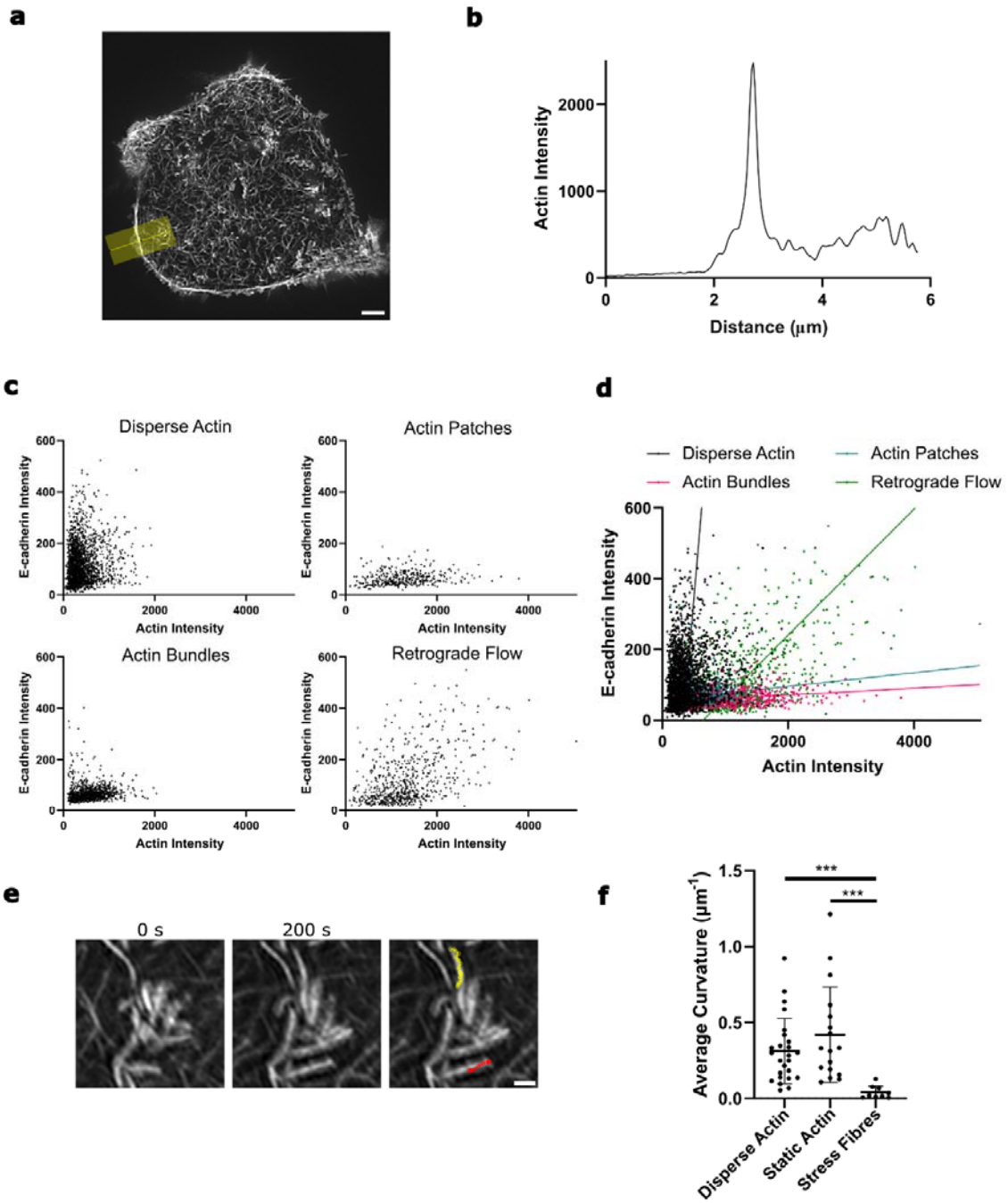

Supp Fig 2: a TIRF-SIM image of an MCF7 cell expressing LifeAct-TagRFPT, showing formation of actin ring. **b** Line scan of actin intensity along region shown in **a**. **c** Intensities of LifeAct-TagRFPT and GFP-E-cadherin in regions of different actin architecture. **d** Deming regression lines showing relationship between actin and E-cadherin intensities in different actin architectures. **e** Static bundles of actin showing extension of bundles (red and yellow lines shown track of the bundle tip over time); scale Bar = 0.5µm. **f** Average curvatures of disperse filaments and static bundles in MCF7 cells plates on E-cadECD SLBs along with stress fibres in MCF7 cells plated on fibronectin-coated glass coverslips.

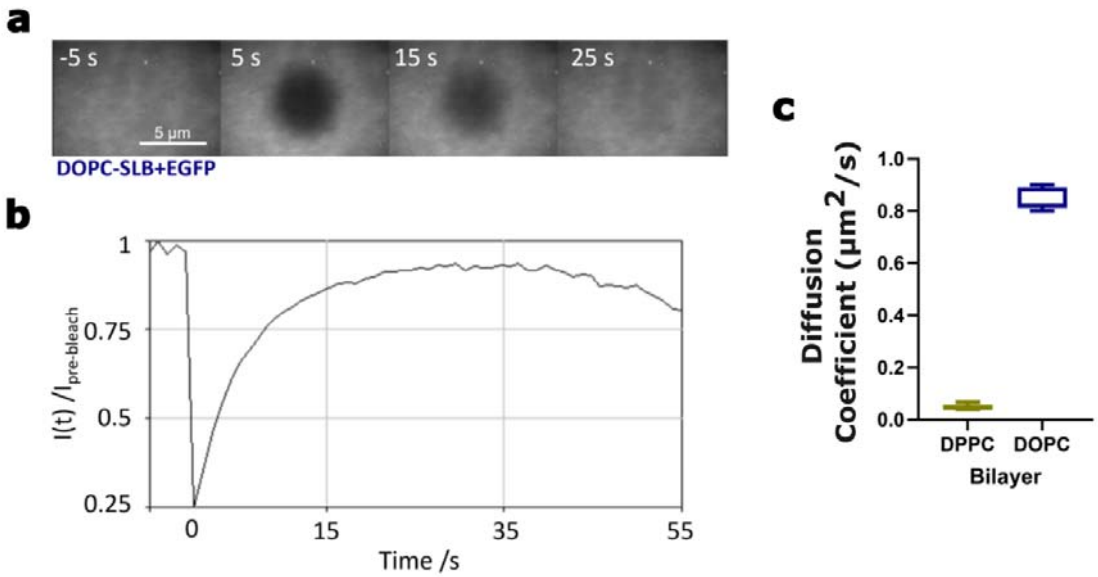

Supp Fig 3: a TIRF Images of DOPC SLBs decorated with EGFP showing fluorescence recovery after photobleaching (FRAP). **b** Intensity plot of fluorescence recovery over time after photobleaching used to calculate diffusion coefficient of the SLB. **c** Diffusion coefficient of DPPC and DOPC SLBs; mean ± SD plotted.

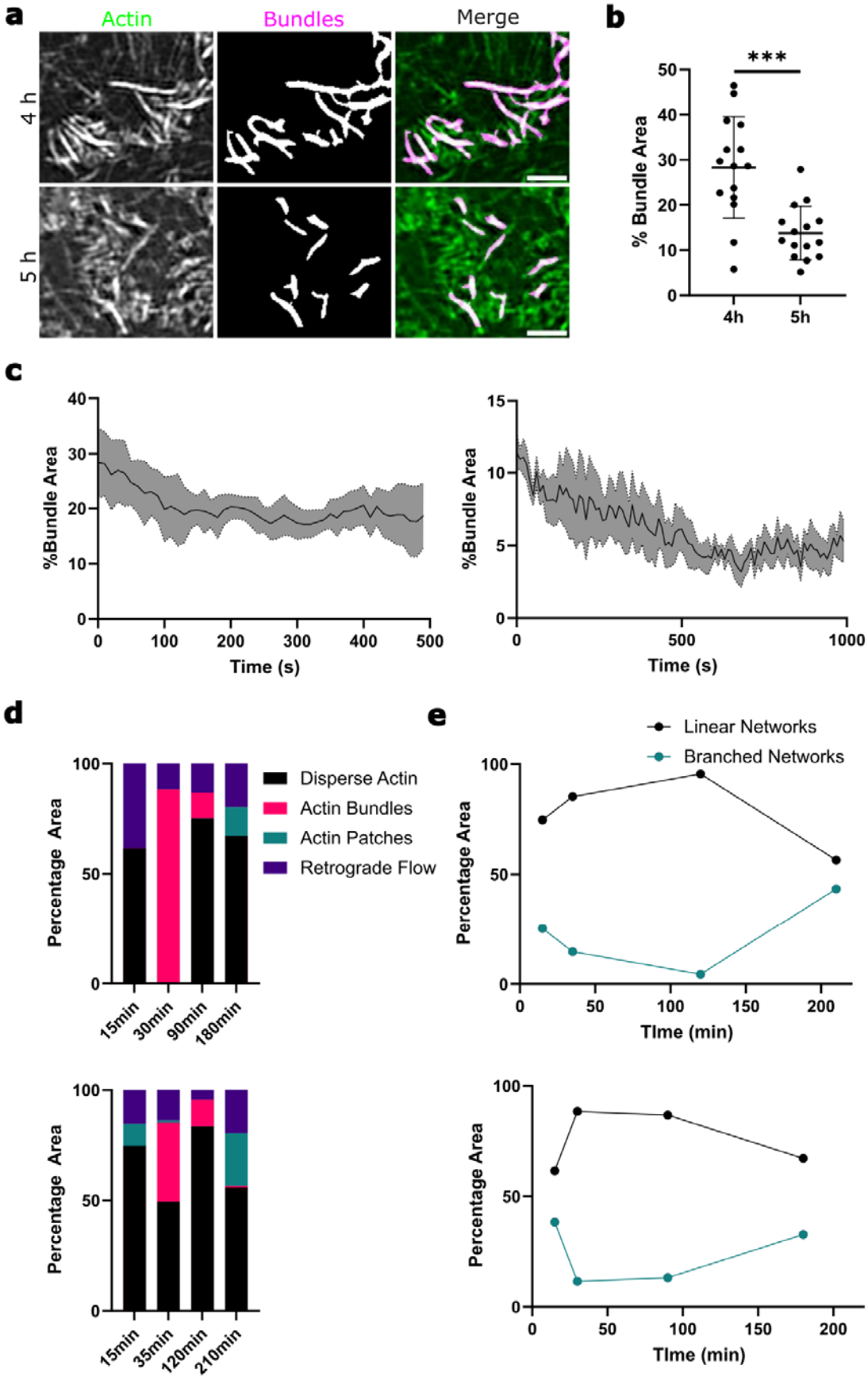
a
Actin
Bundles
Merge
4 h
5 h
b
***
% Bundle Area
4h
5h
c
%Bundle Area
Time (s)
%Bundle Area
Time (s)
d
Percentage Area
Disperse Actin
Actin Bundles
Actin Patches
Retrograde Flow
15min
30min
90min
180min
Percentage Area
15min
35min
120min
210min
e
Linear Networks
Branched Networks
Percentage Area
TIme (min)
Percentage Area
TIme (min)

Supp Fig 4: a TIRF-SIM images of actin and detected bundles within ROIs imaged over shorter time periods; scale Bar = 2µm. **b** % Bundle Area in E-cadherin deficient patches 4 and 5 hours post-seeding; mean ± SD plotted; N=3 **c** Plots showing decrease in % bundle area over time in 2 additional independent repeats; mean ± SD plotted. **d**, **e** Plots showing percentage area covered by different actin architectures and branched and linear actin networks at different times post seeding in 2 additional independent repeats.

References

Abe, Kentaro, and Masatoshi Takeichi. 2008. 'EPLIN Mediates Linkage of the Cadherin–Catenin Complex to F-Actin and Stabilizes the Circumferential Actin Belt'. *Proceedings of the National Academy of Sciences* 105 (1): 13–19. https://doi.org/10.1073/pnas.0710504105.

Achard, Vérane, Jean-Louis Martiel, Alphée Michelot, et al. 2010. 'A "Primer"-Based Mechanism Underlies Branched Actin Filament Network Formation and Motility'. *Current Biology* 20 (5): 423–28. https://doi.org/10.1016/j.cub.2009.12.056.

Acharya, Bipul R., Selwin K. Wu, Zi Zhao Lieu, et al. 2017. 'Mammalian Diaphanous 1 Mediates a Pathway for E-Cadherin to Stabilize Epithelial Barriers through Junctional Contractility.' *Cell Reports* (United States) 18 (12): 2854–67. https://doi.org/10.1016/j.celrep.2017.02.078.

Arslan, Feyza Nur, Julia Eckert, Thomas Schmidt, and Carl-Philipp Heisenberg. 2021. 'Holding It Together: When Cadherin Meets Cadherin'. *Biophysical Journal* 120 (19): 4182–92. https://doi.org/10.1016/j.bpj.2021.03.025.

Arslan, Feyza Nur, Édouard Hannezo, Jack Merrin, Martin Loose, and Carl-Philipp Heisenberg. 2024. 'Adhesion-Induced Cortical Flows Pattern E-Cadherin-Mediated Cell Contacts.' *Current Biology□: CB* (England) 34 (1): 171-182.e8. https://doi.org/10.1016/j.cub.2023.11.067.

Axelrod, D., D. E. Koppel, J. Schlessinger, E. Elson, and W. W. Webb. 1976. 'Mobility Measurement by Analysis of Fluorescence Photobleaching Recovery Kinetics.' *Biophysical Journal* (United States) 16 (9): 1055–69. https://doi.org/10.1016/S0006-3495(76)85755-4.

Bertocchi, Cristina, Yilin Wang, Andrea Ravasio, et al. 2017. 'Nanoscale Architecture of Cadherin-Based Cell Adhesions'. *Nature Cell Biology* 19 (1): 28–37. https://doi.org/10.1038/ncb3456.

Biswas, Kabir H., Kevin L. Hartman, Cheng-han Yu, et al. 2015. 'E-Cadherin Junction Formation Involves an Active Kinetic Nucleation Process.' *Proceedings of the National Academy of Sciences of the United States of America* (United States) 112 (35): 10932–37. https://doi.org/10.1073/pnas.1513775112.

Biswas, Kabir H., Kevin L. Hartman, Ronen Zaidel-Bar, and Jay T. Groves. 2016. 'Sustained α-Catenin Activation at E-Cadherin Junctions in the Absence of Mechanical Force'. *Biophysical Journal* 111 (5): 1044–52. https://doi.org/10.1016/j.bpj.2016.06.027.

Braga, Vania M.M., Laura M. Machesky, Alan Hall, and Neil A. Hotchin. 1997. 'The Small GTPases Rho and Rac Are Required for the Establishment of Cadherin-Dependent Cell–Cell Contacts'. *Journal of Cell Biology* 137 (6): 1421–31. https://doi.org/10.1083/jcb.137.6.1421.

Cavey, Matthieu, and Thomas Lecuit. 2009. 'Molecular Bases of Cell-Cell Junctions Stability and Dynamics.' *Cold Spring Harbor Perspectives in Biology* (United States) 1 (5): a002998. https://doi.org/10.1101/cshperspect.a002998.

Charras, Guillaume, and Alpha S. Yap. 2018. 'Tensile Forces and Mechanotransduction at Cell-Cell Junctions.' *Current Biology□: CB* (England) 28 (8): R445–57. https://doi.org/10.1016/j.cub.2018.02.003.

Collins, Caitlin, Aleksandra K. Denisin, Beth L. Pruitt, and W. James Nelson. 2017. 'Changes in E-Cadherin Rigidity Sensing Regulate Cell Adhesion'. *Proceedings of the National Academy of Sciences* 114 (29): E5835–44. https://doi.org/10.1073/pnas.1618676114.

Friedl, Peter, and Roberto Mayor. 2017. 'Tuning Collective Cell Migration by Cell-Cell Junction Regulation.' *Cold Spring Harbor Perspectives in Biology* (United States) 9 (4). https://doi.org/10.1101/cshperspect.a029199.

Fritzsche, Marco, Alexandre Lewalle, Tom Duke, Karsten Kruse, and Guillaume Charras. 2013. 'Analysis of Turnover Dynamics of the Submembranous Actin Cortex'. *Molecular Biology of the Cell* 24 (6): 757–67. https://doi.org/10.1091/mbc.e12-06-0485.

Grikscheit, Katharina, Tanja Frank, Ying Wang, and Robert Grosse. 2015. ‘Junctional Actin Assembly Is Mediated by Formin-like 2 Downstream of Rac1.’ *The Journal of Cell Biology* (United States) 209 (3): 367–76. https://doi.org/10.1083/jcb.201412015.

Han, Siew Ping, Yann Gambin, Guillermo A. Gomez, et al. 2014. ‘Cortactin Scaffolds Arp2/3 and WAVE2 at the Epithelial Zonula Adherens.’ *The Journal of Biological Chemistry* (United States) 289 (11): 7764–75. https://doi.org/10.1074/jbc.M113.544478.

James, John, Artem I Fokin, Dmitry Y Guschin, et al. 2025. ‘Vinculin–Arp2/3 Interaction Inhibits Branched Actin Assembly to Control Migration and Proliferation’. *Life Science Alliance* 8 (2): e202402583. https://doi.org/10.26508/lsa.202402583.

Jannie, Karry M., Shawn M. Ellerbroek, Dennis W. Zhou, et al. 2015. ‘Vinculin-Dependent Actin Bundling Regulates Cell Migration and Traction Forces.’ *The Biochemical Journal* (England) 465 (3): 383–93. https://doi.org/10.1042/BJ20140872.

Kobielak, Agnieszka, H. Amalia Pasolli, and Elaine Fuchs. 2004. ‘Mammalian Formin-1 Participates in Adherens Junctions and Polymerization of Linear Actin Cables.’ *Nature Cell Biology* (England) 6 (1): 21–30. https://doi.org/10.1038/ncb1075.

Köster, Darius Vasco, Abrar Bhat, Sankarshan Talluri, and Satyajit Mayor, dirs. 2022. *Reconstitution of Membrane-Tethered Minimal Actin Cortices on Supported Lipid Bilayers.* no. 185. United States. https://doi.org/10.3791/63968.

Lee, Natalie K., Ka Wai Fok, Amanda White, et al. 2016. ‘Neogenin Recruitment of the WAVE Regulatory Complex Maintains Adherens Junction Stability and Tension.’ *Nature Communications* (England) 7 (March): 11082. https://doi.org/10.1038/ncomms11082.

Li, Dong, Lin Shao, Bi-Chang Chen, et al. 2015. ‘ADVANCED IMAGING. Extended-Resolution Structured Illumination Imaging of Endocytic and Cytoskeletal Dynamics.’ *Science (New York, N.Y.)* (United States) 349 (6251): aab3500. https://doi.org/10.1126/science.aab3500.

Li, John Xiao He, Vivian W. Tang, Kingsley A. Boateng, and William M. Brieher. 2021. ‘Cadherin Puncta Are Interdigitated Dynamic Actin Protrusions Necessary for Stable Cadherin Adhesion.’ *Proceedings of the National Academy of Sciences of the United States of America* (United States) 118 (24). https://doi.org/10.1073/pnas.2023510118.

Li, John Xiao He, Vivian W. Tang, and William M. Brieher. 2020. ‘Actin Protrusions Push at Apical Junctions to Maintain E-Cadherin Adhesion.’ *Proceedings of the National Academy of Sciences of the United States of America* (United States) 117 (1): 432–38. https://doi.org/10.1073/pnas.1908654117.

Mège, René Marc, and Noboru Ishiyama. 2017. ‘Integration of Cadherin Adhesion and Cytoskeleton at Adherens Junctions.’ *Cold Spring Harbor Perspectives in Biology* (United States) 9 (5). https://doi.org/10.1101/cshperspect.a028738.

Michael, Magdalene, Joyce C. M. Meiring, Bipul R. Acharya, et al. 2016. ‘Coronin 1B Reorganizes the Architecture of F-Actin Networks for Contractility at Steady-State and Apoptotic Adherens Junctions.’ *Developmental Cell* (United States) 37 (1): 58–71. https://doi.org/10.1016/j.devcel.2016.03.008.

Moztarzadeh, Sina, Sara Sepic, Ibrahim Hamad, Jens Waschke, Mariya Y. Radeva, and Alexander García-Ponce. 2024. ‘Cortactin Is in a Complex with VE-Cadherin and Is Required for Endothelial Adherens Junction Stability through Rap1/Rac1 Activation.’ *Scientific Reports* (England) 14 (1): 1218. https://doi.org/10.1038/s41598-024-51269-3.

Noordstra, Ivar, Mario Díez Hermoso, Lilian Schimmel, et al. 2023. ‘An E-Cadherin-Actin Clutch Translates the Mechanical Force of Cortical Flow for Cell-Cell Contact to Inhibit Epithelial Cell Locomotion.’ *Developmental Cell* (United States) 58 (18): 1748-1763.e6. https://doi.org/10.1016/j.devcel.2023.06.011.

Noritake, Jun, Masaki Fukata, Kazumasa Sato, et al. 2004. ‘Positive Role of IQGAP1, an Effector of Rac1, in Actin-Meshwork Formation at Sites of Cell-Cell Contact.’ *Molecular Biology of the Cell* (United States) 15 (3): 1065–76. https://doi.org/10.1091/mbc.e03-08-0582.

Oldenburg, Joppe, Gerard van der Krogt, Floor Twiss, et al. 2015. 'VASP, Zyxin and TES Are Tension-Dependent Members of Focal Adherens Junctions Independent of the α-Catenin-Vinculin Module.' *Scientific Reports* (England) 5 (November): 17225. https://doi.org/10.1038/srep17225.

Oosterheert, Wout, Micaela Boiero Sanders, Johanna Funk, Daniel Prumbaum, Stefan Raunser, and Peter Bieling. 2024. 'Molecular Mechanism of Actin Filament Elongation by Formins'. *Science* 384 (6692): eadn9560. https://doi.org/10.1126/science.adn9560.

Papalazarou, Vassilis, and Laura M. Machesky. 2021. 'The Cell Pushes Back: The Arp2/3 Complex Is a Key Orchestrator of Cellular Responses to Environmental Forces'. *Current Opinion in Cell Biology* 68: 37–44. https://doi.org/10.1016/j.ceb.2020.08.012.

Pollard, Thomas D. 2016. 'Actin and Actin-Binding Proteins.' *Cold Spring Harbor Perspectives in Biology* (United States) 8 (8). https://doi.org/10.1101/cshperspect.a018226.

Reynolds, Albert B. 2010. 'Exposing P120 Catenin's Most Intimate Affair'. *Cell* 141 (1): 20–22. https://doi.org/10.1016/j.cell.2010.03.022.

Schimmel, Lilian, and Ivar Noordstra. 2023. 'Epithelial Cell Spreading Assay on E-Cadherin-Coated Glass or PDMS Substrates for Microscopy-Based Analysis of Cadherin Adhesions'. *STAR Protocols* 4 (4): 102626. https://doi.org/10.1016/j.xpro.2023.102626.

Senju, Yosuke, Toiba Mushtaq, Helena Vihinen, et al. 2023. 'Actin-Rich Lamellipodia-like Protrusions Contribute to the Integrity of Epithelial Cell-Cell Junctions.' *The Journal of Biological Chemistry* (United States) 299 (5): 104571. https://doi.org/10.1016/j.jbc.2023.104571.

Thompson, Connor J., Vinh H. Vu, Deborah E. Leckband, and Daniel K. Schwartz. 2021. 'Cadherin Cis and Trans Interactions Are Mutually Cooperative.' *Proceedings of the National Academy of Sciences of the United States of America* (United States) 118 (10). https://doi.org/10.1073/pnas.2019845118.

Vasioukhin, V., C. Bauer, M. Yin, and E. Fuchs. 2000. 'Directed Actin Polymerization Is the Driving Force for Epithelial Cell-Cell Adhesion.' *Cell* (United States) 100 (2): 209–19. https://doi.org/10.1016/s0092-8674(00)81559-7.

Yamada, Soichiro, and W. James Nelson. 2007. 'Localized Zones of Rho and Rac Activities Drive Initiation and Expansion of Epithelial Cell–Cell Adhesion'. *Journal of Cell Biology* 178 (3): 517–27. https://doi.org/10.1083/jcb.200701058.

Yang, Qing, Xiao-Feng Zhang, Thomas D. Pollard, and Paul Forscher. 2012. 'Arp2/3 Complex-Dependent Actin Networks Constrain Myosin II Function in Driving Retrograde Actin Flow.' *The Journal of Cell Biology* (United States) 197 (7): 939–56. https://doi.org/10.1083/jcb.201111052.

Yao, Mingxi, Wu Qiu, Ruchuan Liu, et al. 2014. 'Force-Dependent Conformational Switch of α-Catenin Controls Vinculin Binding.' *Nature Communications* (England) 5 (July): 4525. https://doi.org/10.1038/ncomms5525.

Yu-Kemp, Hui-Chia, Rachel A. Szymanski, Daniel B. Cortes, et al. 2021. 'Micron-Scale Supramolecular Myosin Arrays Help Mediate Cytoskeletal Assembly at Mature Adherens Junctions'. *Journal of Cell Biology* 221 (1): e202103074. https://doi.org/10.1083/jcb.202103074.